ELSEVIER

Earth and Planetary Science Letters 184 (2001) 407–425

EPSL

www.elsevier.com/locate/epsl

Permeability changes due to mineral diagenesis in fractured crust: implications for hydrothermal circulation at mid-ocean ridges

Fabrice Jh. Fontaine [a,*], Michel Rabinowicz [a], Jacques Boulègue [b]

[a] *Laboratoire de Dynamique Terrestre et Planétaire, UMR 5562, Observatoire Midi-Pyrénées, 14 Avenue Edouard Belin, 31400 Toulouse, France*

[b] *Laboratoire de Géochimie, Physicochimie et Fluides Géologiques, UPMC, UPRESA 7047, 75252 Paris Cedex 05, France*

Received 19 April 2000; accepted 26 October 2000

Abstract

The hydrothermal processes at ridge crests have been extensively studied during the last two decades. Nevertheless, the reasons why hydrothermal fields are only occasionally found along some ridge segments remain a matter of debate. In the present study we relate this observation to the mineral precipitation induced by hydrothermal circulation. Our study is based on numerical models of convection inside a porous slot 1.5 km high, 2.25 km long and 120 m wide, where seawater is free to enter and exit at its top while the bottom is held at a constant temperature of 420°C. Since the fluid circulation is slow and the fissures in which seawater circulates are narrow, the reactions between seawater and the crust achieve local equilibrium. The rate of mineral precipitation or dissolution is proportional to the total derivative of the temperature with respect to time. Precipitation of minerals reduces the width of the fissures and thus percolation. Using conventional permeability versus porosity laws, we evaluate the evolution of the permeability field during the hydrothermal circulation. Our computations begin with a uniform permeability and a conductive thermal profile. After imposing a small random perturbation on the initial thermal field, the circulation adopts a finger-like structure, typical of convection in vertical porous slots thermally influenced by surrounding walls. Due to the strong temperature dependence of the fluid viscosity and thermal expansion, the hot rising fingers are strongly buoyant and collide with the top cold stagnant water layer. At the interface of the cold and hot layers, a horizontal boundary layer develops causing massive precipitation. This precipitation front produces a barrier to the hydrothermal flow. Consequently, the flow becomes layered on both sides of the front. The fluid temperature at the top of the layer remains quite low: it never exceeds a temperature of 80°C, well below the exit temperature of hot vent sites observed at black or white 'smokers'. We show that the development of this front is independent of the Rayleigh number of the hydrothermal flow, indicating that the mineral precipitation causes cold, diffusive vents. Finally, we present a model suggesting that the development of smokers is possible when successive tectonic/volcanic events produce a network of new permeable fissures that can overcome the permeability decrease caused by mineral precipitation. Such a model is consistent with recent seismic data showing hydrothermal vents located at seismologically active ridge segments.

Keywords: hydrothermal vents; convection; porosity; diagenesis

* Corresponding author.

0012-821X/01/$ – see front matter
PII: S0012-821X(00)00332-0

1. Introduction

Since the discovery of the first discharge zone of hot water along the Mid-Atlantic Ridge (MAR) at the Trans-Atlantic Geotraverse (TAG) site [1], numerous scientific investigations as well as submersible campaigns (ALVIN) or drill projects (Ocean Drilling Project) have been conducted to discover new sites and to understand the physical, chemical and biological processes involved in the development of hydrothermal activity. The discovery of vent sites discharging hot fluids is the best evidence of hot hydrothermal activity at ridge crests. The most spectacular examples, called smokers, exhibit temperatures as high as 200–350°C. These smokers are the direct manifestation of fluid venting on the seafloor. Seawater penetrates a permeable system of fissures maintained open by the contraction of the surrounding diabase under stress at ridge crest. Below the top cold horizons, seismic data reveal the existence of magma chambers [2] that supply the heat transported by the hydrothermal convection. Along the 3% of the well-mapped global spreading center [4], hot hydrothermal vent fields are scarce [3]. At slow spreading axes, the location of hydrothermal activity seems to be controlled by well-established crustal fractures like at the TAG site. Hydrothermal sites appear as individual long-lived (10^3–10^4 years) 'mounds' up to several hundred meters in diameter.

The first investigations of the ridge axis along the MAR tended to locate one hydrothermal site every 150–175 km [4]. More recent studies [6] on the active ridge segment at the Azores Triple Junction showed that hydrothermal sites can be much more frequent, i.e., one site every 20–30 km, and intimately linked to ridge segmentation. At fast spreading axes, hydrothermal sites develop along the wall of narrow (about 100 m) axial caldera (like at 9°N along the East Pacific Rise (EPR)). Their characteristic size is about a few tens of meters and their separation length is several meters to several tens of meters. Typically, they last no more than 10–100 years. Nevertheless, they are numerous (45 between 9°27′N and 10°N). Volcanic activity can interact with their evolution. For example, the shorter-lived sites are thought to be the result of sill injection [5], while the older ones are associated with shallow depth of the axial magma chamber. Thus, at fast spreading ridges, hydrothermal activity is intimately associated with volcanic activity. At intermediate spreading ridges, hydrothermal activity ranges from long-lived, fault-bounded, TAG-like hydrothermal systems (e.g., Explorer ridge) to neo-volcanic hydrothermalism (several segments of Juan de Fuca Ridge). Furthermore, many submarine campaigns reveal a diffuse hydrothermal activity with very low-temperature emanations oozing from the crust [5]. When the emanations are geographically associated with mineral deposits, we infer that the hydrothermal system has died. On the other hand, when no minerals are observed, the venting fluid has already precipitated its dissolved minerals inside the crust because of cooling.

Faced with such complex geological problems, numerical models are very helpful to better understand the processes involved. Models assuming hydrothermal flow in a porous medium with a quasi-isotropic permeability distribution allow estimates of heat and mass fluxes at the segment scale [7,8]. Assuming a basal temperature of 500°C, Wilcock [9] found asymptotic exit temperatures consistent with black smokers (sulfide-rich hydrothermal vents with temperatures between 350 and 400°C). He argued that vents with exit temperatures lower than those of black smokers develop if the flow crosses low-permeability crust layers in which the effective local Rayleigh number is reduced. Nevertheless, numerous geological investigations of the seafloor near vent sites show that their localization is related to precise geological features such as bathymetric highs [10] or deformed volcanic blocks near non-transform offsets [6]. Some authors locate them at the intersections of fault and fissure systems [11]. Furthermore, it is well known that animal colonies develop near mineral deposits linked to hydrothermal activity. They often occur on top of fault and fissure systems with high permeability.

Most numerical investigations consider heat transport due to convection in a slot with adia-

batic walls. Recently, Cherkaoui et al. [12] hypothesized that the chronic plume generated during the 1993 diking event along the Coaxial Segment of the Juan de Fuca Ridge was associated with the convective cooling of a 3–5 m wide dike intruded into a 10^{-11}–10^{-12} m^2 cold porous layer. This study shows that vertical advection limits the thermal effects of the dike within a few meters of the dike margins.

A better approach is to address the modeling of convection in a slot surrounded by conductive walls. Such investigations [13] emphasize the role played by the heat absorbed by the walls. This 'horizontal' heat transfer creates a thermal boundary layer inside the wall. Its width increases with time, delaying the onset of convection. Rabinowicz et al. [14] developed a model of convection in a porous slot surrounded by conductive impermeable walls, with realistic equations of state and Rayleigh (Ra) numbers, where seawater enters and leaves the porous medium at its top. Convection occurs as narrow fingers [14]. For $\mathrm{Ra} < 8000$, a thick upper thermal boundary layer develops at the top of the system, while a much thinner one sits on the bottom. Upwelling plumes are able to pierce these cold layers for $\mathrm{Ra} > 8000$, while they are buffered for $\mathrm{Ra} < 8000$. The asymptotic exit temperature of 270°C is similar to that found by Wilcock [9] with adiabatic walls, assuming a basal temperature of 420°C.

At slow spreading centers, hydrothermal activity is driven by magmatic intrusions up to several kilometers in length. The sloping of the basal isotherm due to the three-dimensional geometry of the magmatic intrusions leads to a single-celled flow pattern with upwelling fluids exiting at 370°C. Rabinowicz et al. [14] inferred that black smokers are likely to develop where hydrothermal systems are associated with a tilt of the lower interface, while white smokers (sulfide-poor silica-rich hydrothermal fluids exiting at temperature of 220–350°C) tend to occur above horizontal systems.

We see that hydrothermal systems can generate either white or black smokers. This does not explain why high-temperature vents are so rare [3]. The physical conditions leading to the cold hydrothermal vents [5] remain poorly understood. In the present paper, we show that the sealing of the fracture network due to the precipitation of hydrothermal minerals (anhydrite and sulfides) can lead to cold vents. In Section 2, we describe the model for hydrothermal convection. We also give the equations of state to compute the rate of mineral precipitation/dissolution during convection and derive rules relating the evolution of permeability to diagenesis inside the fault. In Section 3, we describe the evolution of the flow, temperature, and permeability fields resulting from the resolution of the convective equations in a system where permeability evolves with the diagenetic process. The modeling suggests that the diagenesis prevents the development of hot vents. We shall show that this situation is quite general. Significantly, it is also independent of the Rayleigh number of the hydrothermal system. Finally we discuss the processes capable of overcoming the drastic reduction in permeability caused by diagenesis. Such processes are necessary conditions for generation of hot vents.

2. The model

2.1. Physical model

2.1.1. Overall description

To account for the geometry of a kilometer-high hydrothermal system confined to the sheeted dike complex, we consider a faulted zone parallel to the ridge crest bounded by two walls of massive diabase (Fig. 1). The fault is identified with a 'porous slot' containing a system of fissures parallel to the fault axis, with a sub-millimeter aperture δ and separated by meter-scale (spacing f) diabase walls [13,15]. In our model, the xz plane is the fault plane, with the along-strike x axis and the vertical z axis. The y coordinate represents the distance to the central plane of the fault. Due to the symmetry of the system about this central ($y = 0$) plane, we resolve the equations only in the half-space $y \geq 0$. The height of the slot is $H = 1500$ m, its length is $L = 2250$ m and its width is $l = 120$ m. This configuration determines the effective permeability k_{eff} and fracture porosity ε of the network as a function of δ and f:

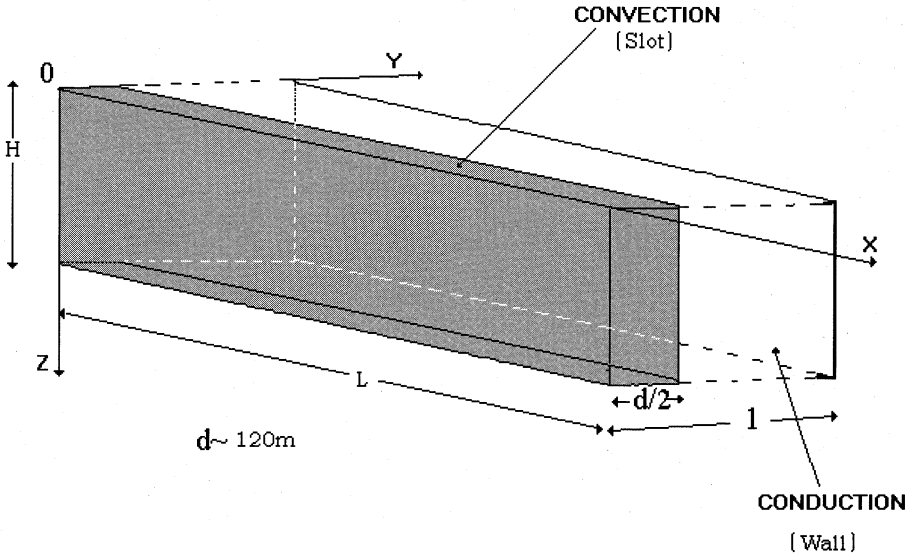

Fig. 1. Geometry of the system. Flow and temperature field are symmetrical on both sides of the $y=0$ axial plane. Equations are resolved in the half-space $y\geq 0$. $L=2.25$ km, $l=0.75$ km, $H=1.5$ km; the thickness of the permeable slot is 120 m.

$$k_{\mathrm{eff}} = \frac{\delta^3}{12f} \tag{1}$$

$$\varepsilon = \frac{\delta}{f} \tag{2}$$

If $\delta=0.1$ mm and $f=1$ m, then $k_{\mathrm{eff}}=10^{-13}$ m^2 while if $\delta=1$ mm, $k_{\mathrm{eff}}=10^{-10}$ m^2; ε ranges between 10^{-4} and 10^{-3}. Although the effective permeability k_{eff} is the only free parameter in our model, it is notoriously difficult to measure in situ. Nevertheless, this range of effective permeabilities includes the lower bound of crustal permeability of 6×10^{-13}–6×10^{-12} m^2 estimated from a potential flow model for the Juan de Fuca hydrothermal vents [16,17]. Moreover, the effective permeability of diabase is about 10^{-18} m^2 [18], i.e., as many as five orders of magnitude smaller than for the fracture network. The permeability of the meter-thick walls between two adjacent fissures is thus negligible. Since the fissures are essentially parallel to the dike plane, the percolation in the y direction is also negligible. Consequently, the circulation is two-dimensional and confined to the xz plane.

The fracture system probably crosses the pillow lavas and the sheeted dike complex over a height of $H=1.5$ km. Large cavities that will ultimately form the stockwork are likely to exist where the fracture system crosses the volcanic extrusives. According to models and data, the effective permeability in the discharge zones inside the pillow lavas before the formation of mineral deposits reaches 10^{-9} m^2 [9,17]. Consequently we consider this upper domain to have a quasi-infinite isotropic permeability.

At the top of the slot, seawater is free to enter at a temperature T of 2°C and to leave with a zero vertical temperature gradient ($\partial T/\partial z=0$) [9]. In our model, the bottom of the slot is held at a constant temperature of 420°C. This temperature is close to the maximum paleo-temperatures of inclusions found in the lower part of the sheeted dike complex which are shown to range between 220 and 430°C [15,19]. It is also colder than the temperature needed to generate a permeable network inside diabases [14]. Hydrothermal flow at high temperatures in the range 420–600°C are known to occur at the ridge crest [15], but they have been associated with the circulation of critical fluids inside the crack network of the isotropic gabbro layer generated during cooling. According to Rovetta [18], the permeability of this

layer is about 10^{-18} m^2. Thus, the associated hydrothermal flow has a low Rayleigh number and the circulation must be very slow. In the upwelling limbs of this hydrothermal flow, the critical fluid precipitates silica particles [20,21] triggered by opal colloids [20]. Since the fluid flow is very slow in the crack network of the gabbro layer, opal transforms into quartz via agglomeration of the colloids [22]. This occludes the crack network and thus destroys the hydrothermal circulation. This sealing effect of silica is very efficient for the isotropic gabbro layer [21].

The interaction of this high-temperature hydrothermal system with that in the sheeted dike complex is naturally weak because the critical point of seawater is about 420°C. At this temperature, two phases coexist: a brine and a fresher component [23]. This is corroborated by the measured salt concentration of the inclusions at temperatures between 220 and 430°C ranging from 10 up to 140 g/l [24]. Due to the relative buoyancy between the two phases, the drops of 'fresh water' move upward, above the interface, and mix with seawater. Consequently, the region below the interface fills completely with brine.

At the interface, surface tension develops between the seawater and the brine. The surface tension of a liquid σ_{liq} enriched or depleted in NaCl as compared to that of seawater σ_{sw} depends on the partial pressure of water above respectively the liquid and seawater at a given temperature. A good approximation is that of regular solutions [25]:

$$\sigma_{liq}-\sigma_{sw}=\left(1-\frac{T}{T_c^{liq}}\right)^{3/2}-\left(1-\frac{T}{T_c^{sw}}\right)^{3/2} \quad (3)$$

where T_c^{liq} and T_c^{sw} are the critical temperatures of the liquid and seawater respectively. For liquids with salinity higher than seawater, we have $T_c^{liq} > T_c^{sw}$, which leads to $\sigma_{liq} > \sigma_{sw}$. This approximation is valid for interfaces of curvature with radius larger than 10 μm. There is an inverse proportionality between the stresses generated by surface tension and the curvature of the interface. Since the curvature of the interface in the direction orthogonal to the sheeted dikes is extremely small (i.e., proportional to the fissure width), the surface tension generates quasi-infinite stresses at the boundary. These stresses inhibit the deformation of both fluids at the interface. Such an effect is equivalent to a step increase of the viscosity of the fluids at the interface and yields to a stratified convection [26]. As a result, the 420°C interface between the brine and seawater corresponds to a deep horizon within the sheeted dike complex. We identify the bottom of our slot with this 420°C interface, but this is not necessarily the bottom of the sheeted dikes.

We assume that the 420°C interface remains in a steady position. This is consistent with the fact that heat is steadily provided by the magma chamber during the early phase of activity of the hydrothermal system. Clearly, when this heat source is exhausted, the transient cooling of the crust causes the fissure network to propagate downward as well as the interface between seawater and the brine. In that case, the hydrothermal system evolves in a way which is completely different from those with a steady bottom [27].

2.1.2. Equations governing convection

In our model, the magnitude of the Darcy velocity (U, 0, W) reaches at most 1 m yr^{-1}, and the minimum grid spacing dz is about 10 m. The time for the fluid to move up by 10 m is about 10 years, much larger than the time necessary to reach a conductive equilibrium between fluid and rock inside the control volume, since $f^2/4\kappa = 3$ days with $\kappa = 10^{-6}$ m^2 s^{-1}. This shows that the temperatures of the solid and the circulating fluid in the fissures are the same. We infer that the temperature governing the fluid and the surrounding conductive basalt is described by:

$$(\rho c)^* \frac{\partial T}{\partial t} + (\rho c)_f \vec{V}\cdot\vec{\nabla} T = \lambda^* \nabla^2 T \quad (4)$$

where $(\rho c)_f$ and $(\rho c)^*$ are the volumetric heat capacity (J m^{-3}) of the fluid and the basalt, respectively; λ^* and $\kappa = \lambda^*/(\rho c)^*$ are the thermal conductivity (J m s^{-1}) and thermal diffusivity (m^2 s^{-1}) of the basalt.

For the flow, Darcy's law is applicable since the real velocity V_{eff}/ε in the fissure network is slow.

We write the velocities in the x and z directions as:

$$U = -\frac{k_{\text{eff}}}{\mu}\frac{\partial p}{\partial x} \quad (5)$$

$$W = -\frac{k_{\text{eff}}}{\mu}\frac{\partial p}{\partial z} + \rho_{\text{f}} g \quad (6)$$

where p is the pressure, μ the fluid viscosity, ρ the fluid density, and g the gravitational acceleration. The density and viscosity of the fluid are taken to be dependent on temperature and pressure. We use the regression of the measured density of a 30 g/l NaCl solution given at each 10 MPa interval [14]. The top pressure is set to 30 MPa. The densities at 30 and 60 MPa are respectively:

$$\rho_{\text{f}} = 1035 - 1415\times10^{-4}\ T - 2384\times10^{-6}\ T^2 \quad (7)$$

$$\rho_{\text{f}} = 1049 - 306\times10^{-4}\ T - 2353\times10^{-6}\ T^2 \quad (8)$$

with T varying between 2 and 420°C.

The viscosity μ(T) is calculated from [14]:

$$\mu = 2.414\times10^{-5}\times10^{\frac{247.8}{T+133}} \quad (9)$$

No pressure and salinity dependences have been taken into account, since their influences are weak in the range of temperatures considered [14].

By neglecting the transient variations of ρ_{f} with time ($\partial\rho_{\text{f}}/\partial t = 0$), we can write the mass conservation equation as:

$$\frac{\partial(\rho_{\text{f}} U)}{\partial x} + \frac{\partial(\rho_{\text{f}} W)}{\partial z} = 0 \quad (10)$$

Thus, introducing the stream function Ψ for steady-state solutions of the flow equation, we can write:

$$U = \frac{1}{\rho_{\text{f}}}\frac{\partial \Psi}{\partial z} \quad (11)$$

$$W = -\frac{1}{\rho_{\text{f}}}\frac{\partial \Psi}{\partial x} \quad (12)$$

2.2. Nature and solubilities of the mineral phases involved in the seawater–crust interactions

2.2.1. Diagenetic processes

The diagenetic processes are triggered by surface reactions between the circulating fluid and the rock walls. They are controlled by the diffusion of the species through the fissures. The diffusivity of the chemical species in seawater for the considered temperatures is about 10^{-8} m^2 s^{-1}. For a fissure width of 0.1 mm, the diffusion time is of the order of 1 s. We will see below (in Section 3) that the thickness of the precipitation front can be as high as 100 m. Since the Darcy velocity in the convective model is relatively small (about 1 m yr^{-1}), the fluid velocity inside the permeable network reaches at most 3×10^{-4} m s^{-1}. Thus, the time needed for the fluid to cross a precipitation front of about 100 m is about 3×10^5 s, about six orders of magnitude larger than the diffusion time of the chemical species inside the fissures. This indicates local equilibrium conditions for the dissolution–precipitation reactions between fluid and rock. Here, we also assume that the minerals which precipitate do not undergo any other chemical reactions.

Finally, we assume that precipitation is triggered when the local concentration exceeds the equilibrium value. Although such a hypothesis is probably wrong, we will show in Section 4 that this simplification does not change our conclusions. Accordingly, at any place in the porous slot, the concentration of any chemical species C is assumed to be the concentration at equilibrium. Thus C satisfies:

$$\rho_{\text{f}}\frac{\text{d}C}{\text{d}t} = \frac{\text{d}m}{\text{d}t} \quad (13)$$

where dm/dt is the rate of mass dissolution or precipitation induced during flow [28].

The concentration depends on both pressure and temperature. Thus, we can write:

$$\frac{\text{d}C}{\text{d}t} = \frac{\partial C}{\partial T}\frac{\text{d}T}{\text{d}t} + \frac{\partial C}{\partial P}\frac{\text{d}P}{\text{d}t} \quad (14)$$

In Section 2.2.3, we will see that sulfide and sulfate minerals predominate as precipitates. The effect of pressure on the solubilities of sulfide and

sulfate minerals has been studied [22,29]. Changes in solubilities due to a variation of pressure of 500 bar are in the same range as changes due to a variation of temperature of 20°C. Hence the effect of pressure is negligible. The pressure effects can be incorporated in the uncertainties of thermodynamic data associated with temperature changes. Therefore:

$$\frac{dC}{dt} = \frac{\partial C}{\partial T}\frac{dT}{dt} \tag{15}$$

Using Eq. 4 we see that the rate of variation of porosity with time $d\varepsilon/dt$ verifies:

$$\frac{d\varepsilon}{dt} = -\frac{\rho_f}{\rho_s}\kappa\frac{\partial C}{\partial T}\nabla^2 T \tag{16}$$

where ρ_s is the mineral density (kg m^{-3}).

2.2.2. Mineral species

According to Alt [30], a hydrothermal system can be divided into three major zones: a recharge zone at the top, a reaction zone at the bottom and a discharge zone at the top. In the recharge zones, 2°C seawater penetrates the crest and is warmed during its descent. At first, pure seawater and rock interact chemically under oxidating conditions and at low temperature (50°C). Then an evolved fluid reacts with the wall in a reductive environment and at higher temperature (200°C).

The chemical reactions in recharge zones are: alkaline earth fixation in the crust, calcite/aragonite precipitation, and anhydrite precipitation. Then the circulation develops in the reaction zones where high-temperature (350–400°C) processes develop. These include sulfur and metals (Fe, Mn) leached from the rock. The warmest hydrothermal solutions, collected at an exit temperature greater than 350°C, are thought to directly come from these zones without any significant cooling [30]. They acquire their chemical and isotopic signature in this reaction zone. Finally, the seawater-rich metals and S circulation reaches the discharge zones where several situations are possible. If the hydrothermal fluid is sufficiently channeled to exit the crust with a low cooling rate, all the mineral content precipitates on the seafloor. The black smokers, whose temperature is greater than 350°C, are the flagrant geological manifestation of this channeling. If the fluid cools inside the crust before exiting, precipitation of the sulfur-bearing minerals (pyrite and chalcopyrite) will happen. When the vent temperature is between 270 and 330°C, white smokers develop. In case of complete cooling inside the crust, all the mineral content of the hydrothermal fluids precipitates in the crust and the resulting hydrothermal manifestation does not deposit mineral on the seafloor [5].

2.2.3. Chemical reactions and rate of precipitation/dissolution

Our model of precipitation/dissolution is based on the mineral solubility calculated from species contained in seawater. To simplify, we restrict our study to the case of a single retrograde and prograde phase. We take anhydrite precipitation/dissolution as the main chemical reaction occurring during seawater heating between 50 and 250°C. Bischoff and Seyfried [31] noticed that the heating of 1 kg seawater forms about 1 g anhydrite ($CaSO_4$). Moreover, $CaSO_4$ is often observed in the oceanic crust samples [30]. Here we consider that the formation of $CaSO_4$ is buffered by the amount of Ca^{2+} contained in seawater. This is roughly one third of the SO_4^{2-} content. The calculated quantity of $CaSO_4$ is about 1.4 g kg^{-1} seawater. Considering that the solubility rate of $CaCO_3$ is one order of magnitude lower than that of $CaSO_4$ we neglect the formation of any calcite or aragonite between 50 and 250°C. Furthermore, we assume that $\partial C/\rho_s \partial T$ is constant.

Accordingly, we find that the value of $\partial C/\rho_s \partial T$ for anhydrite at 50–250°C is:

$$\left(\frac{\partial C}{\rho_s \partial T}\right)_{\text{anhydrite}} = -4.7\times10^{-4}\ ^\circ K^{-1} \tag{17}$$

Outside the temperature interval 50–250°C we assume that $(\partial C/\rho_s \partial T)_{\text{anhydrite}} = 0$. The value in Eq. 17 is likely to be underestimated. During the rock hydrothermal alteration, additional Ca^{2+} is leached from the rock, such that the concentration of precipitated anhydrite is buffered by the SO_4^{2-} in the seawater. This process increases the value of $(\partial C/\rho_s \partial T)_{\text{anhydrite}}$ by a factor 2, favoring

diagenesis. This process is partially compensated by the fact that hydrothermal leaching also increases the fracture porosity.

We chose sulfides as the dominant prograde minerals filling the fissures while the fluid is cooling at 350–250°C. The sulfides are mainly pyrite and chalcopyrite. We assume that the sulfides precipitate in the fissure network. Indeed, basaltic rock contains small quantities of magnetite which react during the hydrothermal alteration with the fluid (HS^-) to produce pyrite. This process germinates in the rock matrix, allowing the sulfides to precipitate in the fissure network. The estimated solubility rate shows that 5 g of sulfides precipitate from 1 kg of seawater in the upwelling [32]. We lower this estimation by considering the precipitation/dissolution of 1 g of sulfides per kg of seawater, to account for the increase in fracture porosity due to the leaching. Thus, the value of $\partial C/\rho_s \partial T$ for sulfides at 250–350°C is:

$$\left(\frac{\partial C}{\rho_s \partial T}\right)_{\text{sulfides}} = 2.4\times10^{-4}\ {}^{\circ}K^{-1} \tag{18}$$

Outside the temperature interval 250–350°C, $(\partial C/\rho_s \partial T)_{\text{sulfides}}$ is assumed to be zero. Finally, we allow the newly formed minerals to dissolve. This is possible when local inversion of the thermal regime between formerly cooling (now warming) and currently warming (now cooling) regions occurs. Precipitation of minerals can cause such an inversion.

We do not consider the formation of silica. The solubility of silica is prograde at temperatures between 25 and 320°C and retrograde above 320°C. Consequently, silica precipitates both in the deepest part of the system, where the fluid is heating, and in upwelling plumes. Silica precipitation occurs in the form of very small opal particles about 5–10 nm in diameter [22]. Their Stokes velocity is negligible (<1 cm yr^{-1}) compared to the fluid velocity in the fissure network. Since opal particles cannot germinate in basaltic rocks, they are flushed outside, where their deposition does not alter porosity in the fractures [28]. This is consistent with the observation of much larger graphite particles of 5–100 μm in size, in hydrothermal vents [33].

2.3. Numerical methods

To resolve the temperature and flow equations, we use non-dimensional equations in the numerical code. The following scaling factors have been used. The unit length scale is $H = 1500$ m. The unit time is $H^2/\kappa = 1.25\times10^5$ years. The unit Darcy velocity is $\kappa/H = 1.2$ cm yr^{-1}. The dimensionless temperature is $\theta = T/\Delta T$, with $\Delta T = 418$°C. The Rayleigh number is defined as:

$$\mathrm{Ra} = \frac{\Delta\rho_f H g k_{\text{eff}}}{\mu_0 \kappa} \tag{19}$$

where μ_0 is the viscosity of seawater at 420°C and $\Delta\rho_f = 440$ kg m^{-3} is the drop in seawater density between 2 and 420°C.

As the effective permeability k_{eff} ranges between 10^{-13} and 10^{-10} m^2, Ra ranges from 1.6×10^4 to 1.6×10^7. Due to computational limitations, we are only able to run cases at the low end of this interval.

Using the previous factors, the dimensionless temperature equation becomes:

$$\gamma\frac{\partial\theta}{\partial\tau} + \vec{V}'\cdot\vec{\nabla}\theta = \nabla^2\theta \tag{20}$$

where τ and $\vec{V}'$ are the dimensionless time and velocity, respectively, and $\gamma = (\rho c)^*/(\rho c)_f = 0.75$ is the ratio of the volumetric thermal capacity of the basalt to that of seawater.

The dimensionless flow equation is:

$$\left(\frac{1}{r}\right)\nabla^2\Psi' = -\left(\frac{\partial}{\partial x'}\left(\frac{1}{r}\right)\frac{\partial\Psi'}{\partial x'} + \frac{\partial}{\partial z'}\left(\frac{1}{r}\right)\frac{\partial\Psi'}{\partial z'}\right) + \mathrm{Ra}\left(\frac{\partial\chi(\theta)}{\partial x'}\right) \tag{21}$$

where x', z' are the dimensionless horizontal and vertical coordinates, respectively, and Ψ' is the dimensionless stream function. The factor r is the dimensionless hydraulic conductivity, $r = R/R_0$. The hydraulic conductivity is defined as $R = k_{\text{eff}}\rho_f g/\mu$ and $R_0 = k_0\rho_0 g/\mu_0$, where $\rho_0 = \rho_f$ (420°C) = 590 kg m^{-3} and $k_0 = k_{\text{eff}}(x', y', z', \tau = 0) = 10^{-13}$ m^2. $\chi(\theta)$ is a dimensionless function scaling the variation of the fluid density which

satisfies:

$$\rho_f(\theta, z') = \rho_0\left(1-\frac{\Delta\rho_f}{\rho_0}\chi(\theta)\right) \quad (22)$$

The dimensionless rate of variation of porosity with time is:

$$\frac{d\varepsilon}{d\tau} = -B\cdot\nabla^2\theta \quad (23)$$

where B is a constant derived from Eqs. 17 and 18.

We used equally spaced points in the x, y, z directions to discretize the equations in the computing box. We have computed the stream function and the temperature in five vertical (xz) planes inside the porous slot while the remaining xz planes are used to describe the wall. For the experiments shown in Fig. 5, for Ra = 8000 and Ra = 12000, we use a set of $(256\times(5+59)\times 256)$ grid points, and a set of $(512\times(5+59)\times 512)$ grid points for Ra = 16000. For the experiments with variable permeability (Figs. 2–6) we use a set of $(192\times(5+59)\times 128)$ grid points. The numerical scheme to solve the flow and temperature equations is given in Rabinowicz et al. [14].

For the experiments with variable permeability (see Section 3.1), at each iteration, we calculate $(\partial/\partial\tau)\varepsilon(x', y', z', \tau)$ the transient rate of variation of the fracture porosity due to anhydrite and sulfides precipitation/dissolution. The evaluation uses Eqs. 17, 18 and 23. These calculations follow the step by step evolution of the fracture porosity field $\varepsilon(x', y', z', \tau)$ inside the permeable slot. Then, using Eqs. 1 and 2, we deduce the permeability field $k_{eff}(x', y', z', \tau)$.

The permeability evolution depending on $\nabla^2\theta$ is a very irregular function. To avoid numerical divergence of the code while resolving the flow equation, we apply a conservative linear filter to the permeability field. For each discrete value of k_{eff}, the filter affects the neighbor values, in a square of dimension 0.03×0.03 (45×45 m). Each of them is weighted with a coefficient inversely proportional to the distance to the central point. This process conserves the mean permeability on a square of (0.03×0.03). Furthermore, we fix a minimum value of $k_0/1000$ for the permeability, also to prevent divergence.

All the experiments begin with a dimensionless thermal regime $\Theta(x', y', z')$ which is a slightly perturbed conductive profile:

$$\Theta(x', y', z') = 1-z' + 2.5\times 10^{-3}\sin(\pi z')A(x', y') \quad (24)$$

where $A(x', y')$ is a random function with unit amplitude.

3. Results

In this section, we first investigate the temporal evolution of the permeability and thermal fields inside the slot while sulfides and anhydrite precipitate and dissolve in the fissure network. Then we attempt to draw phenomenological laws to extrapolate our results to systems with higher Ra numbers.

3.1. Redistribution of porosity due to mineral diagenesis during convection

The computational method to track porosity variations has been described in Section 2.3. The Rayleigh number Ra = 16 000 is consistent with an initial permeability $k_{eff}(x, y, x, t=0) = k_0 = 10^{-13}$ m^2 s^{-1} and an initial fracture porosity $\varepsilon(x, y, z, t=0) = \varepsilon_0 = 10^{-4}$. At the beginning of the experiment (Fig. 2), the circulation along the bottom interface assumes a finger-like structure characteristic of the development of convection in a fault [14]. Such a pattern is expected because of the finite width of the permeable slot. A stagnant volume of cold fluid develops at the top of the slot while hot buoyant plumes are generated at the base. These results are specific to numerical experiments with fluids with temperature-dependent equations of state.

The evolution of the circulation induces a collision between the upwelling hot finger and the initial top stagnant cold sheet of water. In this front, $\nabla^2\theta$ reaches extremely high values, leading to the formation of a front of precipitation. The vertical sheets separating the downwelling and up-

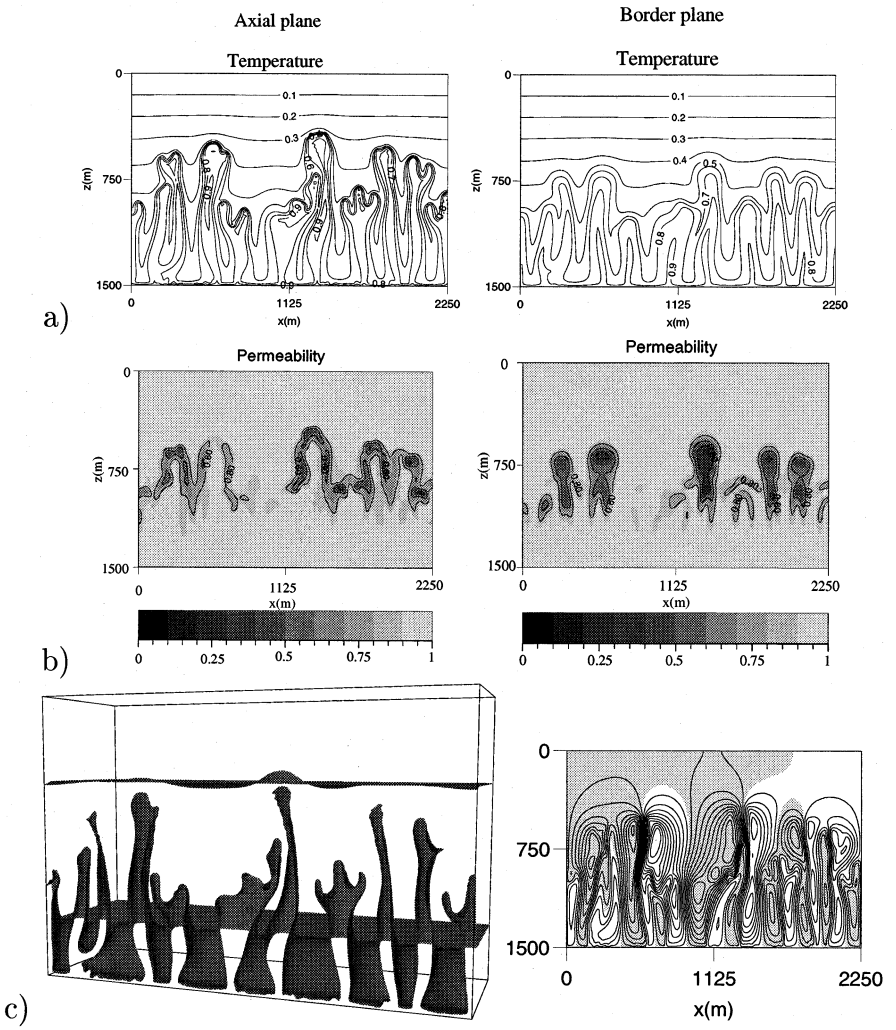

Fig. 2. Snapshot of the dimensionless thermal and permeability fields at the dimensionless time: 6.28×10^{-4} (80 years). In panels a are drawn the temperature fields and in panels b the permeability fields at the axial and border planes of the fault, respectively. The permeability is scaled by $k_0 = 10^{-13}$ m^2; here, between two consecutive isolines the permeability decreases or increases by $0.2k_0$. In panels c the 0.3 (125°C) and 0.8 (335°C) isotherms are represented inside the fault and the wall. Note the finger-like circulation and the viscous fingering. The stream function of the axial plane is also represented: in grayed areas the flow turns clockwise, in white areas the flow turns anticlockwise.

welling plumes lead to the formation of contact zones where strong values of $\nabla^2\theta$ are also ubiquitous. In this zone, significant mineral precipitation (prograde as well as retrograde) along zones of θ gradients occurs. The cores of the ascending plumes are not affected since their temperatures are high enough to avoid mineral precipitation (see Eqs. 17 and 18 for the temperature intervals).

At the axis of the fault, zones of precipitation form thin ribbons at the edges of the ascending fingers (Fig. 2b). The topology of the precipitation domain coupled with the temperature-dependent viscosity favors viscous fingering (Fig. 2c). The low-viscosity hot fluid in the ascending plumes shuns zones where permeability is weak and channels into those where the permeability is good. The temperature gradient across the

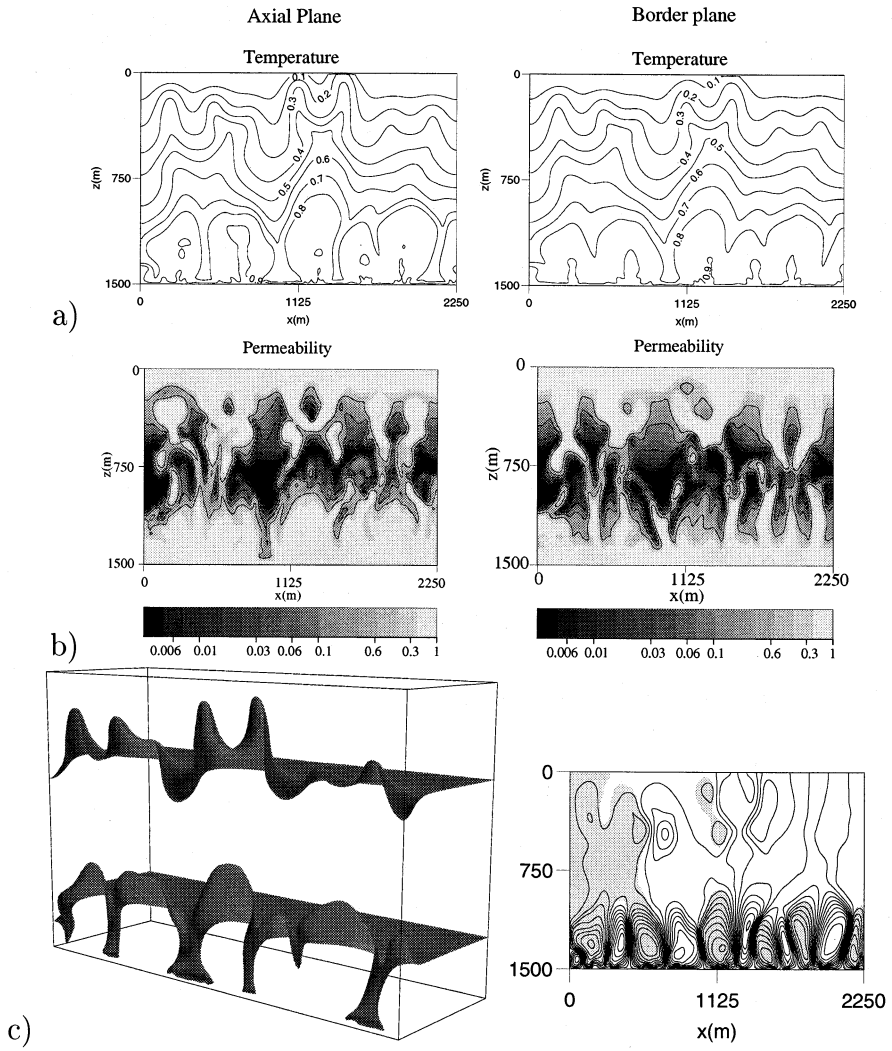

Fig. 3. Same caption and model as in Fig. 2. Snapshot at the dimensionless time: 2.73×10^{-3} (350 years). Venting temperature is about 0.2 (80°C). Between two successive isolines, the permeability drops by a factor $\sqrt{10}$. The minimum of the permeability field is equal to $k_0/300$. Note the complete layering of the circulation.

slot generates fingers which are colder close to the limbs of the fault than on its axis. It also enhances the permeability alteration at the edge of the fault, preventing the development of fingering and weakening the convection. After 80 years, mineral precipitation considerably inhibits the circulation in the whole slot. After 350 years, the finger-like flow is replaced by a diffuse circulation (Fig. 3). The permeability field is strongly reduced in the entire slot, at the axis as well as at the edge of the slot (Fig. 3a,b). The irreversible cooling of the slot generates mineral precipitation everywhere in the slot, except in domains where the temperature is higher than 350°C or lower than 50°C, destroying the finger-like pattern. The thermal fields in the two extreme planes (Fig. 3a) are roughly the same. After 800 years (Fig. 4), the permeability alteration (Fig. 4b) causes a complete layering of the circulation (Fig. 4c): in the lower part of the system convection takes the

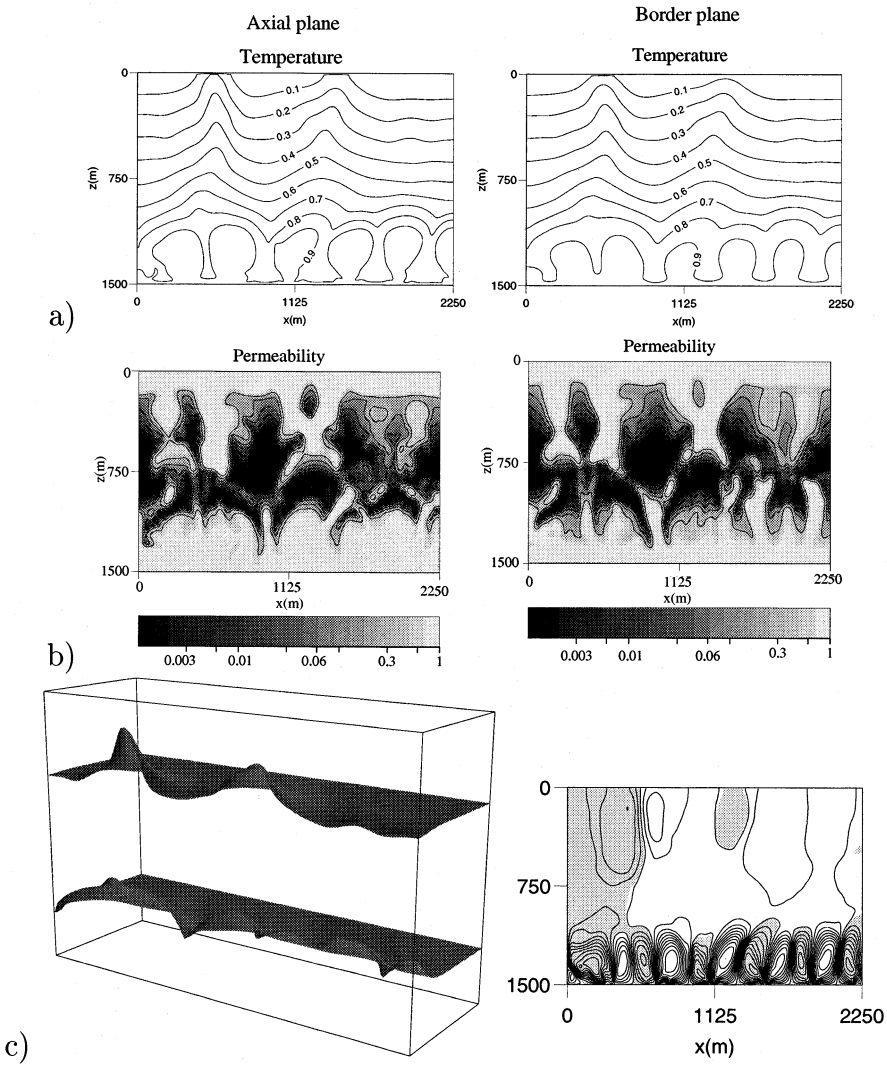

Fig. 4. Same caption and model as in Fig. 2. Snapshot at the dimensionless time: 6.33×10^{-3} (800 years). Dimensionless venting temperature is lower than 0.2 (80°C). Between two successive contours, the permeability drops by a factor $\sqrt{10}$. The minimum of the permeability field is equal to $k_0/1000$.

form of several small regular rolls, while above the front the circulation is very diffuse.

During the whole 8-century duration of the experiment, the venting temperature does not exceed 80°C, well below the inferred 270°C of white smokers (Figs. 2–4). We ran other simulations with different Rayleigh numbers and observed the same phenomenology. This leads to the conclusion that there is a conflict between the growth of the convective instability and the precipitation of minerals in the fissures.

3.2. Influence of Rayleigh number

We have seen that the collision between the hot fingers and the top cold layer generates a precipitation front inside the slot. This collision results from the contrast of buoyancy between hot and

cold fluids: the buoyancy of the layer is proportional to its thermal expansion α ($\alpha = -(1/\rho)\,\partial\rho/\partial\theta$) and to $1/\mu$. The coefficient α increases by a factor 30 from 2 to 420°C (see Eqs. 7 and 8) and μ decreases by about a factor 15 between 2 and 150°C and only by a factor 2 between 150 and 420°C (Eq. 9). The interface between the cold and the hot layers corresponds roughly to the interface between the highly viscous cold layer and the strongly buoyant hot layer. Thus the interface remains between 150 and 250°C (Fig. 5b).

In the following part, we study the evolution of the thermal front as Ra increases. To investigate phenomenological laws, we consider three runs with Ra numbers of 8000, 12 000, and 16 000, in which the permeability of the slot is held constant. At each time step, we compute the maximum positive value of $(\nabla^2\theta)$, $(\nabla^2\theta)_{max}$ in the 50–250°C temperature interval, and the maximum negative value $(\nabla^2\theta)_{min}$ in the 250–350°C interval. These values determine the maximum rate of precipitation of anhydrite and sulfides, respectively. Their temporal evolution is shown in Fig. 5a.

First, we note that $(\nabla^2\theta)_{min}$ is nearly always greater than $(\nabla^2\theta)_{max}$ in absolute value. This shows that in the boundary layers local cooling of the fluid is greater than heating. The evolution of $(\nabla^2\theta)_{min}$ with time can be divided into two main domains: a first one where $(\nabla^2\theta)_{min}$ rapidly increases linearly and a second one where it strongly fluctuates. The fluctuations result from the unsteady nature of the convective circulation. The maximum of the amplitude of $(\nabla^2\theta)_{min}$ as well as the slope in the linear domain clearly increase with Ra. We note that $(\nabla^2\theta)_{min}$ increases as a power of Ra (between 1.5 and 2). This maximum occurs well before fingers can completely erode the cold layer. The dimensionless time

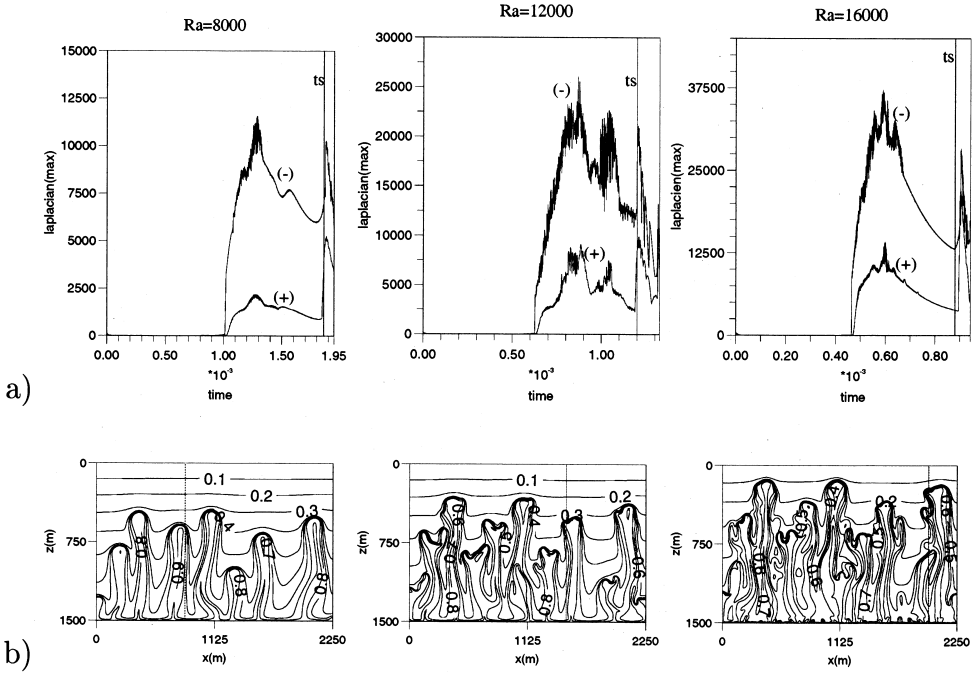

Fig. 5. a: Evolution of $(\nabla^2\theta)_{min}$ and $(\nabla^2\theta)_{max}$ with time for three constant permeability experiments with Rayleigh number Ra = 8000, 12 000, 16 000, respectively. The vertical line (ts) gives the exit time of the fingers. The signs '−' and '+' refer to $(\nabla^2\theta)_{min}$ and $(\nabla^2\theta)_{max}$, respectively. Note that ts exceeds the time when $(\nabla^2\theta)_{min}$ and $(\nabla^2\theta)_{max}$ reach their maxima. b: Thermal field at the axis of the fault taken when $(\nabla^2\theta)_{min}$ reaches its maximum, i.e., 1.3×10^{-3} (160 years), 0.97×10^{-3} (120 years), 0.6×10^{-3} (75 years) for Ra = 8000, Ra = 12 000 and Ra = 16 000, respectively. The vertical line gives the location of the line where $(\nabla^2\theta)_{min}$ is largest in absolute value. Note the development of the extremely narrow thermal boundary layer between hot fingers and top cold water layer.

needed to erode the top cold layers is about 1.85×10^{-3} (230 years), 1.2×10^{-3} (150 years) and 8.8×10^{-4} (110 years) for the three cases where Ra is 8000, 12 000 and 16 000. It indicates that the time needed for the finger to produce hot vents decreases linearly with the Rayleigh number.

As noted in Section 2, the Rayleigh number of a hydrothermal system is poorly known. Rabinowicz et al. [14] have shown that the venting flow rates found at experiments with Ra = 16 000 are compatible with those of hot vents [34]. However, some hydrothermal systems can have Rayleigh numbers three orders of magnitude larger. They are associated with fracture porosity of $\varepsilon = 10^{-3}$ and permeability $k_{\mathrm{eff}} = 10^{-10}$ m^2 [15]. Yet numerical modeling of such cases is clearly beyond today's computers. For the case with Ra = 16 000 and $\varepsilon = 10^{-4}$, we see that the magnitude of the Darcy velocity reaches 1 m yr^{-1}. This corresponds to a fluid velocity $V_{\mathrm{Darcy}}/\varepsilon$ which does not exceed 3×10^{-4} mm s^{-1}. For Ra numbers up to three orders of magnitude larger, the porosity increases by one order of magnitude and the fluid velocity never exceeds a few 10^{-2} m s^{-1}. At this speed, the inertial terms are small, and thus the usual linear version of Darcy's law still applies (see Eqs. 5 and 6). The hypothesis of thermal equilibrium between fissure and walls still holds (see Eq. 4) and local chemical equilibrium between rock and seawater also.

By assuming that the relationship between $(\nabla^2\theta)_{\mathrm{min}}$, the exit time of the fingers and Ra still holds for such high Ra, we can deduce that the rate of precipitation of the mineral increases faster than the residence time of the finger decreases, since it is proportional to $(\nabla^2\theta)$. Accordingly, it is likely that even for Ra numbers up to 1.6×10^7, the sealing of the fissure network prevents the hot fingers from reaching the top of the slot. Thus, the mineral precipitation in the fissures likely prevents the formation of hydrothermal vents, whatever the Ra number is.

4. Discussion

Our conceptual model of hydrothermal circulation at ridge crest consists of a fracture zone of about 100 m surrounded by conductive walls inside the sheeted dike complex. Figs. 2–5 show that the temperature remains low (50–100°C) in a large region near the top of the slot. Because of the temperature-dependent viscosity μ and thermal expansion α, this top cold layer is highly viscous and convectively stable. Along the bottom of the slot, the hot buoyant fingers (low-μ, high-α) have to erode the top cold layer before venting hot fluids onto the seafloor. Yet, this erosion is inhibited by the precipitation of anhydrite and sulfides at the interface between the cold top layer and the fingers. This result is obtained assuming a Ra number of 16 000, and is likely true for Ra up to 10^7. The calculation assumes that the diagenesis occurs at equilibrium.

In our modeling, we adopt a power law relationship between permeability and porosity, assuming that the permeable system consists of perfectly parallel fissures crossing the whole slot. Nature is clearly more complicated. It is more likely that the permeable system consists of a set of fissures generated during micro-seismic events, with a relatively large thickness (up to a few millimeters) [15] and a vertical extent of several meters. In that case, the mean fracture porosity can reach a few percent instead of the 10^{-4} considered here. As a result, the permeability of these systems is not controlled by the mean width of the fissures, but by the effective width of the micro-fissures allowing percolation of seawater from one large fissure to the other. Hence, the relationship between permeability and fracture porosity depends on the effective width of this macro- and micro-fissure network.

A crucial issue is the location where minerals precipitate. If precipitation preferentially occurs within large fissures, it is the fracture porosity deduced from the mean width of the fissures which controls the evolution of permeability during diagenesis. In this case, our modeling shows that the time needed to fill the fissures is long enough to generate hydrothermal vents. Such a situation is probably unlikely. Indeed, we have seen that mineral precipitation is controlled by surface reactions between rock and hydrothermal fluid, especially for sulfides which germinate in the

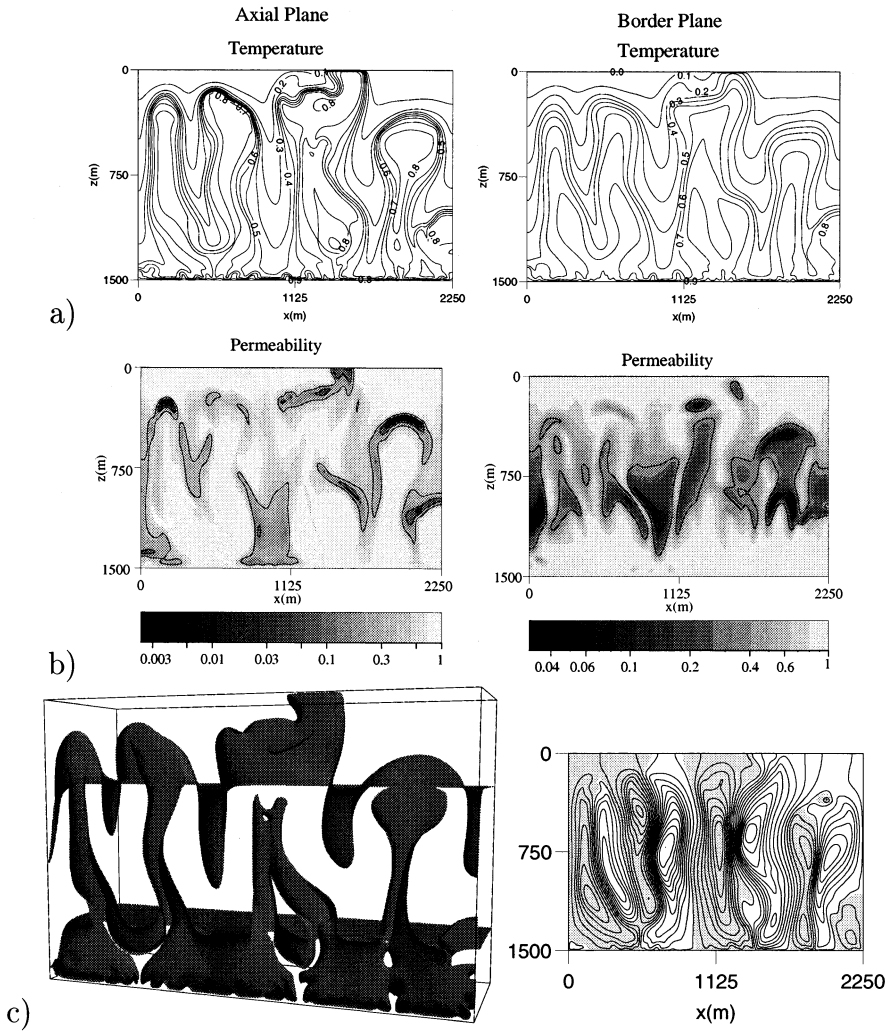

Fig. 6. Same model and caption as in Fig. 2, but re-initialized with the thermal field of Fig. 3 and a constant permeability equal to k_0. The snapshot is taken at time 4.1×10^{-4} (50 years) after the re-initialization. Between two successive contours, the permeability drops by a factor $\sqrt{10}$. Venting temperature reaches $\theta=0.7$ (295°C).

walls of the fissures (Section 2.2.3). Moreover, sulfides precipitate preferentially in constricted zones where the ratio of water to rock is high, thus in the micro-fissures. This localized precipitation hardly affects the large fissures but seals the micro-fissures. Such a process reduces permeability as fast as in our models.

Another important point is the need for notable supersaturation to trigger mineral precipitation, particularly for sulfides. Supersaturation localizes precipitation in narrow temperature domains. It likely accelerates the obstruction of the permeable network, and thus favors the rapid sealing of the system. We argue that the seawater hydrothermal system in diabases lines micro-fissures with minerals just as cholesterol hardens arteries. Another possibility is that the precipitation triggered by supersaturation occurs as clots which occlude the micro-fissures, as during a heart attack. In both cases, the mineral precipitation prevents the development of hot vents, while a precipitation of mineral restricted to the large fissures leads

to hot vents. Hence, the occasional occurrence of hydrothermal vents is a strong argument in favor of rapid occlusion of the permeable network by hydrothermal flows at ridge axes.

To explain the occurrence of hot vents, we imagine a process generating a new permeable system. We run a case beginning with the 350-year-old thermal field of the model of Figs. 2–4. In this experiment the initial permeability is reset to $k_0 = 10^{-13}$ m^2, and the Rayleigh number is 16 000. After 50 years, the hot fingers buffered at mid depth below the precipitation front rapidly move upward and exit through the top of the slot with a temperature of 295°C (Fig. 6). The circulation maintains this exit temperature for 50–70 years: Thereafter, it slowly decreases by about 2°C yr^{-1}. Thus, recovering permeability can generate vents.

Several processes can be evoked to explain such a permeability recovery. A first hypothesis consists of thermo-elastic cracking during the transient cooling of the fracture [35]. We do not think that this process is very efficient in our case, because the whole system tends to warm up during the short time necessary to form the precipitation front. This prohibits contraction of the matrix. Nevertheless, thermo-elastic stresses may be efficient once the system is cooling, i.e., as the hydrothermal process is dying. Contraction may then open new pathways to fluid circulation. However, the modeling of hydrothermal systems during the transient cooling of the crust is too complicated to be addressed in the present paper, as stated in Section 1.

We also suggest that local seismic events at the ridge crest can create a new permeable system allowing fluid circulation. The ridge crust is host to a number of dynamic processes that are able to create micro-earthquakes. Among them are diking events, tectonic faulting, and thermal strain [36]. To generate an earthquake, crustal temperatures must be low enough to allow brittle deformation, and stresses must exceed the local rock strength. At slow spreading ridges (≤ 4 cm yr^{-1}), seismic hypocenters have been located 7–8 km under the seafloor [37]. This indicates that fault slip can occur over relatively large areas, generating earthquakes with $m_b \geq 4.5$ and even teleseismic events [38]. Many of them are due to normal fault slip [37]. Such seismic events in the vicinity of a sealed hydrothermal system may be responsible for the permeability recovery of the model of Fig. 6.

Extensive circulation inside the new fissure network generates hot vents which vent fluids at 270–290°C over times as long as a century. If the permeability of this vent is periodically renewed (every 50–100 years), i.e., if the same fault slips repeatedly, the vent can exit fluid continuously at temperatures of 270–290°C for as long as a thousand years with little variation in the vent exit temperature. Otherwise, the hot discharges (with temperatures of 220–290°C) last between two and three centuries. On slow spreading axes, diking events occur once every 50–100 years on average on active segments, for about 8 km of axial valley. Seismic swarms may also re-open the fissures and drive hydrothermal circulation as described before.

Another way to favor the formation of vent field is to start the convective process from a different thermal regime than that considered here. We think that the intrusion of magmatic body, such as sills, in the crust can lead to a 'pre-heating' of the slot, which would decrease the thermal shock by reducing the temperature contrast between the fault and the walls. The cooling of a meter-thick intrusion will not contribute to heat efficiently a 100-m-wide fracture. A particularly significant magmatic intrusion, about 10 m thick as possibly at hot spot sites, would be required to promote an appreciable heating of the fracture.

The situation is quite different on axes spreading faster than 10 cm yr^{-1}. On the EPR, the depth range of the micro-earthquakes suggests brittle behavior restricted to the first 1–2 km of the crust [36]. This explains why moderate earthquakes ($m_b \geq 1$) are not observed on fast spreading axes. The small earthquakes appear to be the result of stresses generated by thermal contraction of the basalt as it cools [36]. Studies have resolved the structure of young upper crust at the EPR at 9°30′N [39]. The results suggest that dike intrusions reach within a few hundred meters below the seafloor. Moreover, Haymon et al. [5] postulated that hydrothermal activity develops near the tops of these intrusions. More recently, the mod-

eling of Rabinowicz et al. [14] indicated that the time scale required for the development of such 100-m-high hydrothermal systems is about a few years instead of the 10^3 years for 1.5-km-high systems. The characteristics (temperature field and mass/heat flux exiting the system) of the circulation depend on the Rayleigh number and not on the height of the system. On this basis, Rabinowicz et al. [14] infer that the numerous short-lived black and white smokers in the Northern Pacific [40,41] are likely associated with such shallow intrusions. The characteristics of the model of Figs. 2–5 apply to such a shallow hydrothermal system. Furthermore, these small seismic events are several orders of magnitude more frequent than the more important ones at slow spreading axes. These suffice to renew permeability in a hydrothermal system with a height of a few hundred meters. Thus, we think that the discussion for slow spreading axes also holds for fast spreading ridges, but at a shorter time scale.

The study and observation of seismic activity on ridge crests are recent [42] and the links between hydrothermal system and seismic activity are not well understood yet. Information about the recurrence of diking events on a given piece of ridge must improve our knowledge of tectonic, volcanic and hydrothermal processes.

5. Conclusion

We have modeled the influence of diagenetic permeability changes on hydrothermal circulation. Rabinowicz et al. [14] have described the convective process and thermal regime in a vertical slot surrounded by conductive walls assuming a basal temperature of 420°C. In this study, we simulate the evolution of the permeability field resulting from the precipitation of anhydrite and sulfides in the fissure network. We assume local equilibrium between the mineral phases and the crust. Some 1.4 g of anhydrite and 1 g of sulfides per kg of seawater are likely to form during a convective cycle.

The experiments show the development of a transition which transforms the initial conductive regime in an asymptotic one with finger-like plumes exiting hot fluids. During this transition, (1) a thermal shock between hot rising fingers and top cold stagnant water layers induces a front of precipitation at notable depth below the top of the slot, (2) thereafter, the front gradually thickens, and (3) the decrease of the permeability in the front leads to a layering of the hydrothermal flow on both sides of the front: in the bottom layer the temperature is too high (>350°C) and in the top layer the fluid temperature is too low (<50°C) for mineral diagenesis to develop. As a consequence, venting temperatures are low (<80°C) and well below the values observed at white or black smokers.

Our models indicate that the great drop in seawater viscosity around 150°C coupled with the strong increase of the thermal expansion with temperature explains the development of the front. We show that the rate of precipitation of minerals increases more rapidly with Ra than the time needed for the fingers to produce hot vents decreases. This suggests that our results can plausibly be extended to higher Ra numbers.

We show that if we reset the permeability field to its initial value, the fingers rapidly reach the top and generate white smokers. We think that seismic activity near sealed hydrothermal systems may create the permeability recovery necessary to drive the formation of hot vents. Diking events may also favor the formation of hot vents by decreasing the temperature contrast between the walls and the fracture, by pre-heating the whole system. Recent seismic surveys of ridge crest must improve our knowledge of the interactions between hydrothermal systems and volcanic/seismic activity by determining the periodicity of diking and microseisms on the same ridge portion.

Acknowledgements

We wish to thank Pierre Genthon for his stimulating discussions during this work, Anne Briais for helpful information, Kurt Feigl for English improvements and the reviewers Abdellah Cherkaoui and Frank Spera for their constructive suggestions. The computations were supported by the Centre National d'Etudes Spatiales (CNES). This

work has been funded by the ECODEV program.*[AC]*

References

[1] P.A. Rona, B.A. Macgregor, P.R. Betzer, G.N. Bolger, D.C. Krause, Anomalous water temperature over the Mid-Atlantic Ridge crest at 26°N latitude, Deep Sea Res. 22 (1975) 611–618.
[2] J.M. Sinton, R.S. Detrick, Mid-Ocean ridge magma chamber, J. Geophys. Res. 97 (1992) 197–216.
[3] A.C. Campbell, M.R. Palmer, G.P. Klinkhammer, T.S. Bowers, J.M. Edmond, J.R. Lawrence, J.F. Casey, G. Thompson, S. Humphris, P. Rona, J.A. Karson, Chemistry of hot springs on the Mid-Atlantic Ridge, Nature 335 (1988) 514–519.
[4] E.T. Baker, C.R. German, H. Elderfield, Hydrothermal plumes over spreading-center axes: Global distributions and geological inferences, in: S.E. Humphris et al. (Eds.), Seafloor Hydrothermal Systems: Physical, Chemical, Biological and Geological Interactions within Submarine Hydrothermal Systems, Geophys. Monogr. Ser. 91, AGU, Washington, DC, 1995, pp. 47–71.
[5] R.M. Haymon, D.J. Fornari, M.H. Edwards, D. Wright, K.C. Macdonald, Hydrothermal vents distribution along the East Pacific Rise (9°09′–54′N)and its relationship to magmatic and tectonic processes on fast spreading mid-ocean ridge, Earth Planet. Sci. Lett. 104 (1991) 513–534.
[6] C.E. German, L.M. Parson, HEAT Scientific Party, Hydrothermal exploration at the Azores Triple Junction: Tectonic controls of venting at slow-spreading ridges? Earth Planet. Sci. Lett. 138 (1996) 93–104.
[7] N.J. Rosenberg, F.J. Spera, Role of anisotropic and/or layered permeability in hydrothermal system, Geophys. Res. Lett. 17 (1990) 235–238.
[8] B.J. Travis, D.R. Janecky, N.D. Rosenberg, Three-dimensional simulations of hydrothermal circulation at mid-ocean ridges, Geophys. Res. Lett. 18 (1991) 1441–1444.
[9] W.S.D. Wilcock, Cellular convection models of mid-ocean ridge hydrothermal circulation and the temperature of black smokers fluids, J. Geophys. Res. 103 (1998) 2585–2596.
[10] B.J. Murton et al., Direct evidence for the distribution and occurrence of hydrothermal activity between 27° and 30°N on the Mid-Atlantic Ridge, Earth Planet. Sci. Lett. 125 (1994) 119–128.
[11] J.A. Karson, P.A. Rona, Block-tilting, transfer faults, and structural control on magmatic and hydrothermal processes in the TAG area, Mid-Atlantic Ridge 26°N, Geol. Soc. Am. Bull. 102 (1990) 1635–1645.
[12] A.S.M. Cherkaoui, W.S.D. Wilcock, Thermal fluxes associated with the 1993 diking event on the Coaxial segment, Juan de Fuca Ridge: a model for the convective cooling of a dike, J. Geophys. Res. 102 (1997) 24887–24902.
[13] C. Tournier, P. Genthon, M. Rabinowicz, The onset of natural convection in vertical fault planes: consequences for the thermal regime in crystalline basements and for heat recovery experiments, Geophys. J. Int. 140 (2000) 500–508.
[14] M. Rabinowicz, J.C. Sempéré, P. Genthon, Thermal convection in a vertical permeable slot: Implications for hydrothermal circulation along mid-ocean ridges, J. Geophys. Res. 104 (1999) 29275–29292.
[15] P. Nehlig, Fracture and permeability analysis in magma-hydrothermal systems transition zones in the Samail Ophiolites (Oman), J. Geophys. Res. 99 (1994) 589–601.
[16] W.S.D. Wilcock, A. McNabb, Estimates of crustal permeability on the Endeavour segment of the Juan de Fuca mid-ocean ridge, Earth Planet. Sci. Lett. 138 (1996) 83–91.
[17] A.T. Fisher, Permeability within basaltic oceanic crust, Rev. Geophys. 36 (1998) 143–182.
[18] M.R. Rovetta, A similarity model of incremental fracture growth in submarine hydrothermal systems, J. Geophys. Res. 98 (1993) 4173–4182.
[19] D.S. Kelley, K.M. Gillis, G. Thompson, Fluid evolution in submarine magma-hydrothermal systems at the Mid-Atlantic Ridge, J. Geophys. Res. 98 (1993) 19579–19596.
[20] J.T. Wells, M.S. Ghiorso, Coupled fluid flow and reaction in mid-ocean ridge hydrothermal systems: the behavior of silica, Geochim. Cosmochim. Acta 55 (1991) 2467–2481.
[21] J.T. Martin, R.P. Lowell, Precipitation of quartz during high temperature, fracture-controlled hydrothermal upflow at ocean ridges: Equilibrium versus linear kinetics, J. Geophys. Res. 105 (2000) 869–882.
[22] H.D. Holland, S.D. Malinin, The solubility and occurrence of non-ore minerals, in: H.L. Barnes (Ed.), Geochemistry of Hydrothermal Ore Deposits, John Wiley, New York, 1979, pp. 461–508.
[23] J.L. Bischoff, R.J. Rosenbauer, An empirical equation of state for hydrothermal seawater (3.2 wt% NaCl), Am. J. Sci. 285 (1985) 725–763.
[24] P. Nehlig, T. Juteau, V. Bendel, J. Cotten, The root zones of oceanic hydrothermal systems: constraints from the Samail ophiolite (Oman), J. Geophys. Res. 99 (1994) 4703–4713.
[25] R. Defay, I. Prigogine, Surface Tension and Adsorption, Longmans, London, 432 pp.
[26] H.C. Nataf, S. Moreno, P. Cardin, What is responsible for thermal coupling in layered convection?, J. Phys. France 49 (1988) 1707–1714.
[27] S. Schoofs, F.J. Spera, U. Hansen, Chaotic thermohaline convection in low-porosity hydrothermal systems, Earth Planet. Sci. Lett. 174 (1999) 213–229.
[28] M. Rabinowicz, J.L. Dandurand, M. Jakubowski, J. Schott, J.P. Cassan, Convection in a North Sea oil reservoir: inferences on diagenesis and hydrocarbon migration, Earth Planet. Sci. Lett. 74 (1985) 387–404.
[29] H.L. Barnes, Solubilities of ore minerals, in: H.L. Barnes (Ed.), Geochemistry of Hydrothermal Ore Deposits, John Wiley, New York, 1979, pp. 404–460.
[30] J.C. Alt, Sub-seafloor processes in Mid-Ocean Ridge hydrothermal system, in: S.E. Humphris et al. (Eds.), Sea-

floor Hydrothermal Systems: Physical, Chemical, Biological and Geological Interactions within Submarine Hydrothermal Systems, Geophys. Monogr. Ser. 91, AGU, Washington, DC, 1995, pp. 85–114.
[31] J.L. Bischoff, W.E. Seyfried, Hydrothermal chemistry of seawater from 25°C to 350°C, Am. J. Sci. 278 (1978) 838–860.
[32] M. Rabinowicz, J. Boulègue, P. Genthon, Two- and three-dimensional modeling of hydrothermal convection in the sedimented Middle Valley segment, Juan de Fuca Ridge, J. Geophys. Res. 103 (1998) 24045–24065.
[33] J. Jedwab, J. Boulègue, Graphite crystals in hydrothermal vents, Nature 310 (1984) 41–43.
[34] M.K. Tivey, Modeling chimney growth and associated fluid flow at seafloor hydrothermal vent sites, in: S.E. Humphris et al. (Eds.), Seafloor Hydrothermal Systems: Physical, Chemical, Biological and Geological Interactions within Submarine Hydrothermal Systems, Geophys. Monogr. Ser. 91, AGU, Washington, DC, 1995, pp. 158–177.
[35] L.N. Germanovich, R.P. Lowell, Percolation theory. Thermoelasticity, and discrete hydrothermal venting in the earth's crust, Science 255 (1992) 1564–1567.
[36] R.A. Sohn, J.A. Hildebrand, S.C. Webb, A microearthquake survey of the high-temperature vent fields on the volcanically active East Pacific Rise (9°50′N), J. Geophys. Res. 104 (1999) 25367–25378.
[37] L.S.L. Kong, S.C. Salomon, G.M. Purdy, Microearthquake characteristics of a mid-ocean ridge along-axis high, J. Geophys. Res. 97 (1992) 1659–1685.
[38] P.Y. Huang, S.C. Salomon, E.A. Bergman, J.L. Nabelek, Focal depths and mechanisms of Mid-Atlantic Ridge earthquakes from body waveform inversion, J. Geophys. Res. 91 (1986) 579–598.
[39] G.L. Christeson, G.M. Purdy, G.J. Fryer, Structure of young upper crust at the East Pacific Rise near 9°30′N, Geophys. Res. Lett. 19 (1992) 1045–1048.
[40] D.J. Fornari, R.W. Embley, Tectonic and volcanic controls on hydrothermal processes at the Mid-Ocean ridge: an overview based on near-bottom and submersible studies, in: S.E. Humphris et al. (Eds.), Seafloor Hydrothermal Systems: Physical, Chemical, Biological and Geological Interactions within Submarine Hydrothermal Systems, Geophys. Monogr. Ser. 91, AGU, Washington, DC, 1995, pp. 1–46.
[41] P. Gente, J.M. Auzende, V. Renard, Y. Fouquet, D. Bideau, Detailed geological mapping by submersible of the East Pacific Rise axial graben near 13°N, Earth Planet. Sci. Lett. 78 (1986) 224–236.
[42] G.C. Fox, In situ observations of the onset of hydrothermal discharge during 1he 1998 eruption at Axial Volcano, Geophys. Res. Lett. 26 (1999) 3445–3448.